

Optimal metrology with variational quantum circuits on trapped ions

Christian D. Marciniak^{1,*}, Thomas Feldker^{1,*}, Ivan Pogorelov¹, Raphael Kaubruegger^{2,3}, Denis V. Vasilyev^{2,3}, Rick van Bijnen^{2,3}, Philipp Schindler¹, Peter Zoller^{2,3}, Rainer Blatt^{1,2}, and Thomas Monz^{1,4†}

¹ Institut für Experimentalphysik, 6020 Innsbruck, Austria

² Institute for Quantum Optics and Quantum Information, 6020 Innsbruck, Austria

³ Center for Quantum Physics, 6020 Innsbruck, Austria and

⁴ Alpine Quantum Technologies (AQT), 6020 Innsbruck, Austria

(Dated: July 6, 2021)

Cold atoms and ions exhibit unparalleled performance in frequency metrology epitomized in the atomic clock. More recently, such atomic systems have been used to implement programmable quantum computers and simulators with highest reported operational fidelities across platforms. Their strength in metrology and quantum information processing offers the opportunity to utilize tailored, programmable entanglement generation to approach the ‘optimal quantum sensor’ compatible with quantum mechanics. Here we report quantum enhancement in metrology beyond squeezing through low-depth, variational quantum circuits [1] searching for optimal input states and measurement operators in a trapped ion platform. We perform entanglement-enhanced Ramsey interferometry finding optimal parameters for variational quantum circuits using a Bayesian approach to stochastic phase estimation tailored to the sensor platform capabilities and finite dynamic range of the interferometer. We verify the performance by both directly using theory predictions of optimal parameters, and performing online quantum-classical feedback optimization to ‘self-calibrate’ the variational parameters. In both cases we find that variational circuits outperform classical and direct spin squeezing strategies under realistic noise and imperfections. With 26 ions we achieve 2.02(8) dB of metrological gain over classical interferometers.

I. INTRODUCTION

Leveraging quantum mechanics to push beyond the boundaries classical physics imposes on metrology is a pursuit that has seen advances over many decades [2–5]. A natural question that arose is what the optimal method would be to perform measurements aiming to estimate a parameter as precisely as possible. The notion of optimality is always relative to something. It is inevitably linked to a cost function which quantifies distance to the state which can no longer be improved without relaxing constraints imposed on it. A key challenge is thus to identify, and with a given set of available, constrained resources also implement experimentally, the optimal measurement procedure.

A seminal example for parameter estimation is Ramsey interferometry, where the goal is to learn a phase ϕ encoded in a quantum superposition of two states. The question of optimality has been answered in this setting when we are restricted to classical resources only: The variance of the phase estimation is bounded by the standard quantum limit (SQL) [6]. We can utilize entanglement to relax the constraint of classical resources to go beyond the SQL, as discussed in the context of squeezed state interferometry [3, 7–9], and Greenberger–Horne–Zeilinger (GHZ) interferometry [4, 10]. In particular, GHZ states have been identified as optimal quantum states for Ramsey interferometry, saturating the Cramér–Rao bound [11, 12]. They thus provide the

best possible outcome compatible with quantum mechanics, that is the precision is only bounded by the Heisenberg limit (HL).

However, GHZ interferometry has decisive shortcomings. Apart from these states being exceedingly sensitive to experimental imperfections which can negate any advantage over classical metrology [13], the notion of optimality for GHZ interferometry is constrained to be local. This technique is optimal only for a particular phase value that must be chosen a priori. Its optimal performance as measured by a cost function is restricted to an exceedingly small region around this value, and this region becomes smaller at the same rate as the variance. Thus, using many entangled probes in this fashion enables super-classical estimation in the immediate vicinity of one phase value only. In contrast, many applications like atomic clocks require estimation of a stochastically varying phase in a single measurement with little a priori knowledge of its value. In this case, one must extend the notion of optimality for a finite dynamical range [14] of the phase to be measured.

Here we demonstrate optimal metrology with finite dynamic range using low-depth variational quantum circuits on a programmable, trapped-ion quantum sensor [1]. These variational circuits generate input states and measurement operators which are optimal with respect to a sensing-task-specific cost function under a given set of sensor resources and constraints. We utilize a Bayesian approach to stochastic parameter estimation which is naturally well-suited for sensing tasks such as in atomic clocks. We show that the circuits presented herein run on current NISQ-era machines with solely collective control, provide metrologically relevant gains, and are

* These authors contributed equally to this work

† thomas.monz@uibk.ac.at

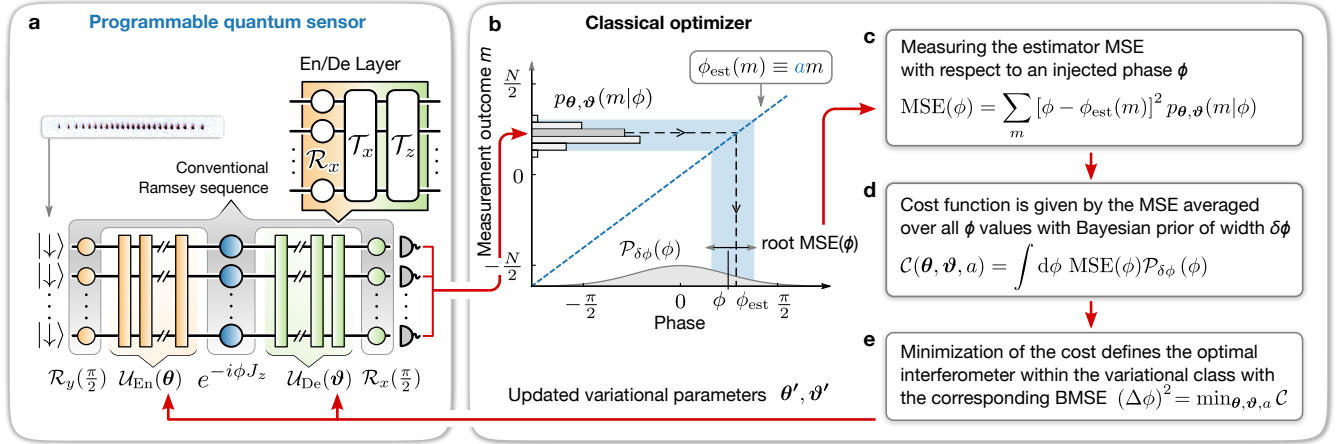


Figure 1. Measurement and feedback concept for variational quantum Ramsey interferometry circuits. **a** A programmable quantum sensor executes a generalized Ramsey sequence with entangling and decoding unitaries \mathcal{U}_{En} , and \mathcal{U}_{De} . The unitaries are made from a repeating sequence of sensor resource gates, here collective qubit rotations $\mathcal{R}_{x,y,z}$, and infinite-range one axis twistings $\mathcal{T}_{x,y,z}$ with parameter sets $\{\theta, \vartheta\}$. **b** The measurement outcomes m from the the quantum sensor are used to produce an estimate of the phase ϕ with prior distribution $\mathcal{P}_{\delta\phi}$ using a linear phase estimator ϕ_{est} with slope a . **c** The conditional probabilities $p_{\theta, \vartheta}(m|\phi)$ obtained from a measurement record may be used to define a mean square error with respect to the true phase and the used estimator. **d** An operational cost function \mathcal{C} can be defined to quantify the interferometer performance for a variational sequence parameter set $\{\theta, \vartheta\}$. **e** Minimization of the cost function is achieved by determining new parameter sets $\{\theta', \vartheta'\}$ and comparing the associated costs either on-device or using classical simulation.

robust to realistic noise and imperfections. We demonstrate this using two complementary approaches: First, capitalizing on the high levels of control in trapped-ion systems we directly implement variational quantum circuits using theory predictions for interaction parameters. Second, we utilize an on-device quantum-classical feedback optimization of the circuit to ‘self-calibrate’ the variational parameters in the regime where manual calibration is challenging.

Measurement scheme and phase estimation

We illustrate such optimal metrology by performing generalized multi-particle Ramsey interferometry as a pertinent application. In a classical metrology setting a Ramsey sequence (Fig. 1 a) operates on a single or a collection of uncorrelated particles. In such clocks measurement outcomes m are the differences of particles in the two projected eigenstates providing access to the system magnetization. This magnetization together with a phase estimator $\phi_{\text{est}}(m)$ is used to obtain a phase estimate, which allows shot-per-shot feedback, stabilizing the clock at resonance.

Extending this strategy, we first generalize the Ramsey sequence with additional, variational unitary operations we refer to as *entangling* and *decoding* unitaries (Methods M1 for details). The variational entangling operation prepares states tailored to a sensing task and platform, while the decoding prepares an optimal measurement operator for a given sensing task, input state, and sensor properties. These unitaries, \mathcal{U}_{En} and \mathcal{U}_{De} , are

added before and after the free Ramsey phase evolution, respectively (Fig. 1 a, also Eq. 1 in M1), and represent low-depth variational circuit approximations to the optimal interferometer unitaries [15], given a suitable cost function and constraints.

The entangling and decoding unitaries consist of a layered sequence of sensor resource gates (Eqs. 2 - 3), that are characterized by their number of layers n_{En} and n_{De} , and two parameter vectors θ and ϑ . Here, these resource gates are collective Rabi oscillations (qubit rotations) and operations, commonly called infinite-range one axis twisting (OAT) [16] interactions due to their action on the Bloch sphere, which are available in many atomic or trapped ion systems [17, 18] (see M1 Eqs. 4 - 5). Measurements outcomes of the sequence are used together with a linear estimator function ϕ_{est} to generate a phase estimate (Fig. 1 b) analogously to the standard Ramsey approach.

The second discerning feature here is how we quantify the change in uncertainty of the phase through measurement. In static phase estimation this is regularly done by defining a mean square error (MSE, Fig. 1 c and Eq. 6 in M1). However, in stochastic parameter estimation, and in particular in the context of optimization, this is not a suitable strategy (Methods M1). Instead, we use a Bayesian approach to stochastic phase estimation which makes use of the knowledge (or uncertainty) of the value of the phase *before* the measurement, which determines the so-called *prior* distribution. Measurements are then used to perform Bayesian updates of the prior yielding the *posterior* distribution, which provides an estimate of the post-measurement uncertainty. This posterior dis-

tribution is related to the Bayesian mean square error (BMSE) [19]. The BMSE is an integral quantity (see M1 Eqs. 7 and 9) that weighs phases by importance based on the interferometer dynamic range and sensitivity (remarks Methods M1). It only depends on variational parameters, and sensor properties (see M2) via the prior distribution, and thus lends itself to define a cost function (Eq. 8) to optimize the variational circuit with (Fig. 1 d - e). The minimum of the BMSE cost function with respect to the variational parameters is here denoted by $(\Delta\phi)^2$.

For successfully optimized sequences the prior width $\delta\phi$ (Eq. 7) is closely related to the interferometer *dynamic range* [14], within which ϕ_{est} performs faithfully. The BMSE can be linked to the amount of (Fisher) information extracted per shot from the measurement [12, 15]. In atomic clocks the BMSE can be linked additionally to the Allan variance σ (M3), where the prior width is a power-law function of both the present noise bandwidth b_α [20, 21] and the free Ramsey evolution time T_R .

We implement the optimal Ramsey interferometry above on a compact trapped-ion quantum computing platform [22]. This platform is used as a programmable quantum sensor, where in this work a linear chain of up to 26 $^{40}\text{Ca}^+$ ions is hosted in a Paul trap. Optical qubits are encoded in the ground state $|4\text{S}_{1/2}, m_J = -1/2\rangle$ and excited state $|3\text{D}_{1/2}, m_J = -1/2\rangle$, which are connected via an electric quadrupole clock transition near 729 nm. Technical details of the implementation can be found in the Supplementary Material, in particular state preparation and readout (S1), implementation and calibration of unitaries via the Mølmer-Sørensen interaction (S2), and technical restrictions imposed on the scheme (S3).

II. RESULTS

We study the performance of the variationally optimized Ramsey sequences for four different choices of entangling and decoding layer depths ($n_{\text{En}}, n_{\text{De}}$) generating four distinct circuits: (0, 0) being a classical coherent spin state (CSS) interferometer [12] as the baseline comparison. All other sequences have been variationally optimized, (1, 0) being similar to a squeezed spin state (SSS) interferometer [12], (0, 2) with a CSS input state and tailored measurement, and finally (1, 2) with both tailored input and measurement.

Direct implementation of theory parameters

Following the execution of a Ramsey sequences (Eq. 1 in M1 or S2) we perform projective measurements at different Ramsey phases ϕ to reconstruct the expectation value of the total spin z projection, J_z (Fig. 2 a). From the measurements we construct the MSE (Fig. 2 b) using the linear estimator function $\phi_{\text{est}} = am$ with slope a which minimizes the cost function \mathcal{C} obtained

from integration according to Eq. 8 (see remarks in M1, and S4 and Tab. 1). Qualitatively, Ramsey sequences with input state squeezing ($n_{\text{En}} > 0$) dip below the CSS around $\phi = 0$ as seen in Fig. 2 b. This dip is a manifestation of reduced projection noise. Sequences with optimized measurement operators ($n_{\text{De}} > 0$) exhibit a broader range of ϕ values for which the MSE is comparable to the $\phi = 0$ value. This is a consequence of the enhanced dynamic range that the non-trivial decoding unitaries impart, that is, the range over which the expectation value $\langle J_z \rangle / \hbar$ remains well-approximated by the linear estimator (Fig. 2 a). Combining tailored input and measurements ($n_{\text{En}}, n_{\text{De}} > 0$) yields an MSE which is both lower and wider than the CSS baseline.

To study this behaviour quantitatively as a function of the prior width $\delta\phi$ and particle number N we calculate the Bayesian mean square error from the MSE, scaled to the prior width $\delta\phi$ used. This is a convenient measure since $\delta\phi$ encapsulates *prior* knowledge of ϕ and $\Delta\phi$ encapsulates *posterior* knowledge after measurement. Their ratio $\Delta\phi/\delta\phi$ is therefore bounded on the interval $[0, 1]$. We investigate this quantity for $\delta\phi \in [0.2, 1]$ rad as a representative sample of the parameter space, since no information is gained as $\delta\phi \rightarrow 0$ or π (Fig. 2 c).

All variationally optimized sequences outperform the CSS within this measure (Fig. 2 c). The effect of change in dynamic range is evident in the location of a sequence's minimum. Minima of sequences with decoding layers shift towards larger prior widths (longer T_R) with respect to the CSS, while for the direct spin-squeezing (1, 0) it shifts towards smaller values. Sequences with a larger number of operations deviate more strongly from the theory predictions due to accumulation of gate errors. This behaviour is consistent across a range of particle numbers (Fig. 2 c inset). The deviation decreases as the system size does. We attribute this to the decrease in the fidelity of entangling operations [22]. The (1, 2) scheme outperforms all others despite the increased complexity. In particular, it outperforms the simple spin-squeezing (1, 0) scheme at both the optimal $\delta\phi$ for (1, 2) and (1, 0), as summarized in Tab. I for two ion numbers.

$\delta\phi$	$N = 12$		$N = 26$	
	0.6893	0.792	0.5480	0.7403
(0, 0)	-3.56(3) dB	-3.63(8) dB	-3.22(3) dB	-4.53(3) dB
(1, 0)	-4.61(12) dB	-4.34(4) dB	-5.63(7) dB	-5.39(2) dB
(1, 2)	-5.06(11) dB	-5.18(8) dB	-5.84(9) dB	-6.75(2) dB

Table I. Comparison of measured values of $\Delta\phi/\delta\phi$ at two values of $\delta\phi$ corresponding to the minima of the (1, 0) (smaller $\delta\phi$) and (1, 2) (larger $\delta\phi$) scheme, respectively. Note that the location of the minimum for (1, 2) and (0, 0) is identical to within the measurement resolution presented.

For atomic clock settings $\Delta\phi$ alone does not capture all relevant processes quantitatively. Consequently, we compute the Allan deviation of a deadtime-free clock (M3) given the same raw data, as shown in Fig. 2 d.

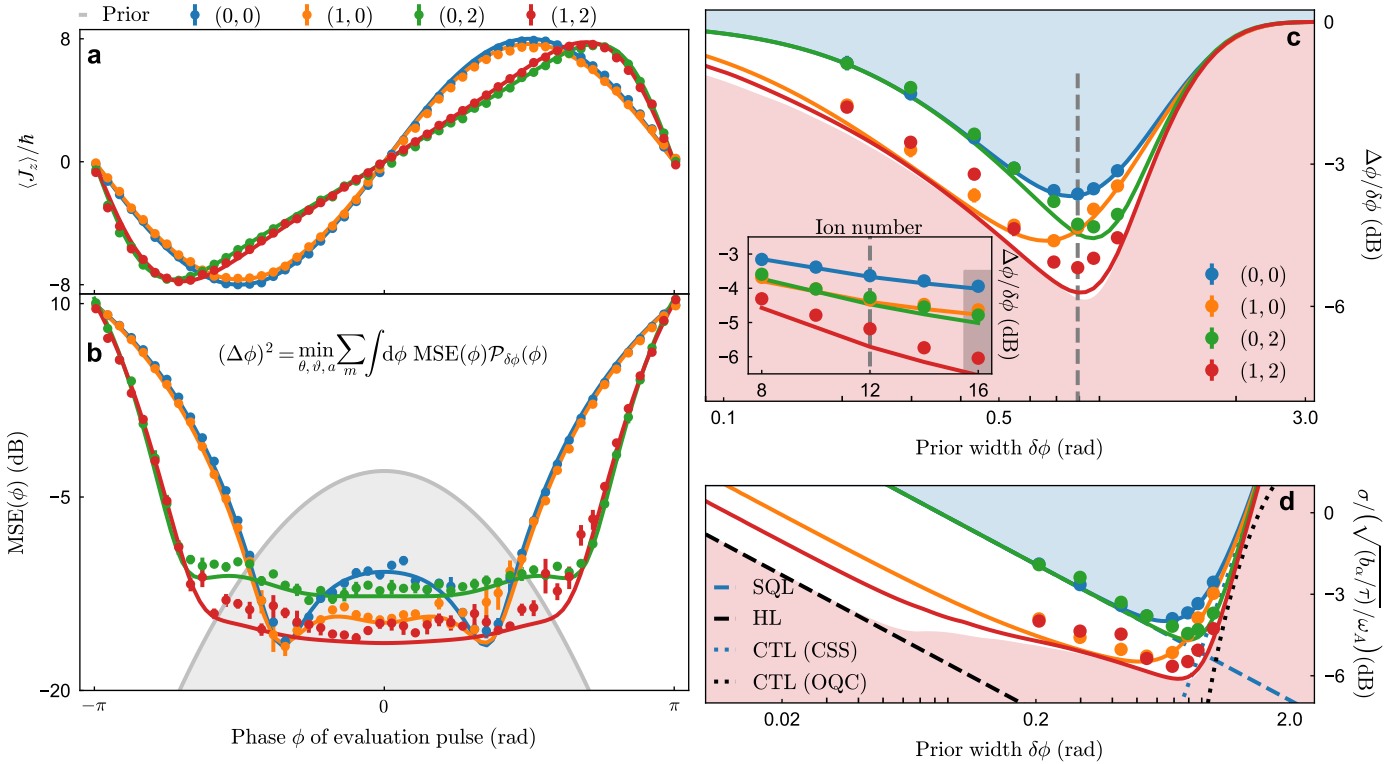


Figure 2. Generalized Ramsey sequence performance measurements. Markers are experimental data with 1σ statistical uncertainties, and solid lines are theory with no free parameters. **a** 16 ion chain expectation value of spin operator $\langle J_z \rangle / \hbar$ as a function of evaluation pulse phase ϕ . 50 experiments are averaged per point, and 5 full traces are recorded to calculate mean and standard deviation of each curve. **b** MSE calculated from traces in **a** for optimal linear estimator ϕ_{est} . Overlaid in grey is the prior distribution $\mathcal{P}_{\delta\phi}(\phi)$ with $\delta\phi \approx 0.79$ (minimum of BMSE vs $\delta\phi$). **c** $\Delta\phi/\delta\phi$ as a function of prior width $\delta\phi$ for 12 ions in the four variational sequences. The blue shaded region corresponds to all classically obtainable values. The red shaded region is inaccessible using this scheme, where the boundary corresponds to the optimal quantum interferometer [15]. Each point is produced by numerically integrating curves as in **b** over ϕ as per Eq. 6. **Inset** $\Delta\phi/\delta\phi$ as a function of particle number at the prior width indicated by the dashed line. $N = 16$ points calculated from data in **b**. **d** Allan deviation normalized to noise bandwidth b_α , averaging time τ and reference frequency ω_A as a function of prior width with coherence time limits (CTL) for CSS and optimal quantum clock (OQC) (dashed lines) indicated along with standard quantum limit (SQL) and Heisenberg limit (HL) (dotted lines) (Methods M3). Raw data, color scheme, and markers from **c**.

On-device quantum-classical feedback optimization

We continue to investigate the parameter ‘self-calibration’ of the scheme in a regime where manual calibration is challenging, such that we expect direct application of theoretically optimal angles to no longer perform well. In particular, this is a regime where accurately calibrating the twisting parameters in $(\boldsymbol{\theta}, \boldsymbol{\vartheta})$ is no longer feasible. Minimization of the cost function is therefore achieved by a feedback loop where a classical optimization routine calculates the cost, and proposes new parameter sets to trial based on measurements performed on the quantum sensor. We employ a global, gradient-free optimization routine with an internal representation or ‘meta-model’ of the cost function (S5).

The meta-model uses the known structure of the resource operations to learn an estimate of the cost function landscape based on the measurements, as seen in Fig. 3 **a** for a 26 ion chain and the (1, 2) circuit. Calibra-

tion of twisting angles is performed at a lower ion number (20), and then approximately scaled to the larger number. The cost function estimates are below the competing CSS (0, 0) and direct spin-squeezing (1, 0) after ≈ 20 measurements despite this lack in accurate calibration. A full iteration of the algorithm is completed after ≈ 50 measurements in Fig. 3 **a**.

Measurement points that the algorithm deems promising candidates for a minimum are resampled using ‘fine’ scans (S6). Fine scans serve to increase the algorithm’s confidence about predictions made on sparse data by better sampling, and relaxing symmetry assumptions of ‘coarse’ scans. Fine scans show convergence towards the theory optimum as the algorithm progresses (Fig. 3 **b**). Convergence is achieved more rapidly for the (1, 0) sequence (Fig. 3 **c**) due to the lower number of variational parameters, and consequently smaller parameter space. This convergence in both sequences despite the inability to accurately calibrate is a manifestation of the op-

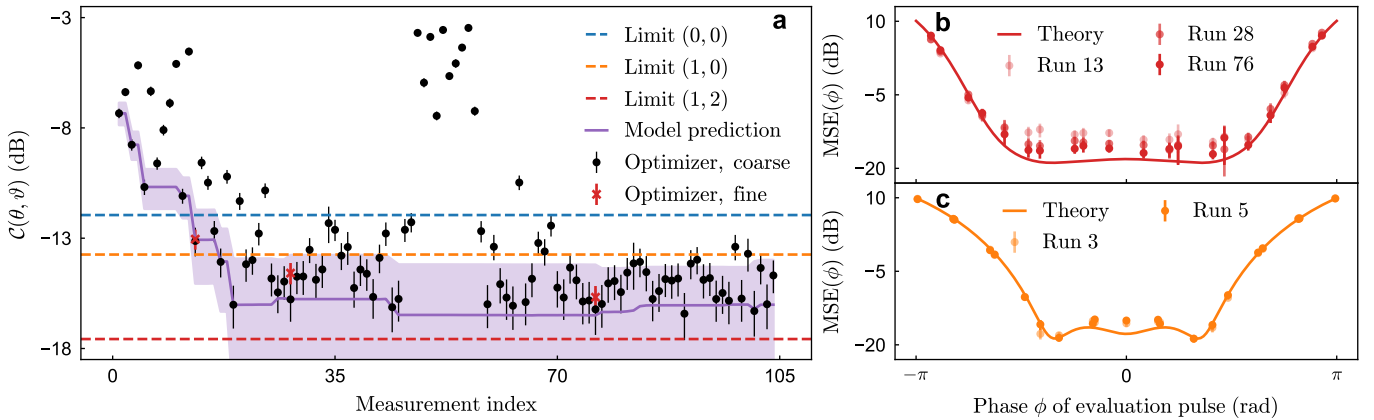


Figure 3. On-device hybrid quantum-classical optimization performance with 26 ions at $\delta\phi \approx 0.74$ (minimum BMSE vs $\delta\phi$), all error bars are 1σ statistical uncertainties. **a** Optimizer cost function C as a function of measurement index (runs). Estimate is based on integration using 10 Hermite-Gauss nodes (S4) and 100 repetitions per point. Dashed lines indicate the achievable performance with the indicated sequences. Red crosses correspond to the automated fine scans displayed in panel **b**. **b** Automated fine scans (S) of the MSE with 20 nodes and 250 repetitions for three measurement indices. **c** Analogous fine scans from optimizer run using (1, 0) sequence. Estimates based on 21 nodes and 250 repetitions per point.

timizer's ability to learn and correct for correlated gate (calibration) errors.

Frequency estimation

All measurements up to this stage were taken by driving rotations $\mathcal{R}_y(\phi)$ with resonant laser pulses as a consequence of our technical implementation (S2). This allows for deterministic mapping of the ϕ space, but in atomic clock experiments the phase ϕ would instead be imparted by the residual detuning of the drive from the atomic reference under the influence of noise. To gauge the performance of a clock we perform frequency estimation experiments. We calculate the variance of the frequency estimator from the known injected noise for a standard CSS interferometer, and the (1, 2) interferometer optimized for a prior width $\delta\phi \approx 0.69$ (S7).

The optimized sequence outperforms the CSS for all considered Ramsey times (Fig. 4). In particular, this demonstrates robustness of the scheme with respect to variations in the prior width (Ramsey time, S8). The deviation between experiment and theory predictions can be explained by two observations. First, we independently measured predominantly frequency flicker noise of bandwidth $b_\alpha \approx 2\pi \cdot 6$ Hz (S7) on the laser which is not present in the simple simulation. Second, the MSE used in the simulation is the ideal, theoretically-achievable one, while the experiment has deviations from the theory such as in Fig. 2 b. Simulating the metrology experiments with these additional noise sources restores good match between data and prediction. We note that this problem is not apparent in the BMSE or the Allan variance plots (Fig. 2 c and d) since it arises solely in the \mathcal{R}_z operation we employ here, while ϕ was imparted via

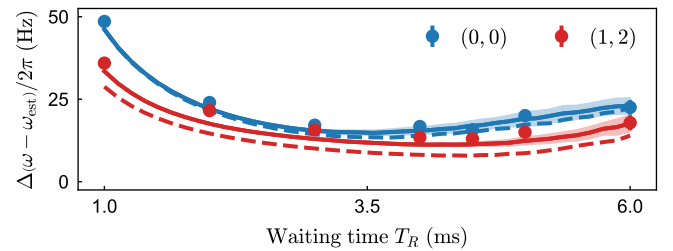


Figure 4. Frequency measurement using 12 ions with a standard and variationally optimized Ramsey sequence. Shown is the standard deviation of the difference between known injected and estimated frequency detuning. Markers are experimental data with uncertainty (finite sampling and projection noise). Dashed lines are theory simulations with no free parameters, while solid lines are simulation of measurement performance including a residual laser flicker noise of $b_\alpha \approx 2\pi \cdot 6$ Hz, and shading indicates error margin of simulation.

\mathcal{R}_y there.

III. DISCUSSION AND OUTLOOK

The measurements we present show that the scheme's increase in sequence complexity does not negate the gains over more straight-forward interferometers. In particular, performance can be maintained even in the presence of gate (calibration) errors.

For realistic metrology settings several other aspects of the scheme are beneficial: It extends the interferometer dynamic range, which in atomic clocks increases the optimal Ramsey time T_R at a fixed noise level. Longer Ram-

sey times can further increase the duty cycle of atomic clocks which reduces the optical Dick effect [23, 24].

In settings where particle number is, to an extent, a free parameter there are two features to highlight. First, one can leverage the scheme’s increased gains with system size. Our demonstration’s implementation of the OAT through the axial mode Mølmer-Sørensen interaction limits us to particle numbers of order 30. However, other trapped-ion OAT implementations e.g. using optical dipole forces in Penning traps used for precision sensing do not suffer this shortcoming. The same holds true in cold atom experiments such as optical lattice clocks, which have recently shown entanglement-enhancement through squeezing [17]. In Tab. II we show the potential gain of the scheme for 12 and 26 ions as demonstrated here compared to 362 atoms as in Ref. [17].

N	Approach	(1, 0)	(1, 2)
12	Theory	1.49(0) dB	2.13(0) dB
	Direct	1.38(1) dB	1.75(2) dB
26	Theory	2.12(0) dB	2.70(0) dB
	Direct	1.47(8) dB	2.02(8) dB
	Optimizer	1.54(9) dB	1.77(8) dB
362	Theory	4.53(0) dB	7.50(0) dB

Table II. Gain over CSS in Allan deviation for 12 and 26 ions (theoretical and closest-measured value of $\delta\phi$) and 362 atoms (theoretical) for two different interferometer states at their respective optimal prior widths (Ramsey times).

The metrological gain in the clock setup can be increased by 3 dB by using the slight additional resource

overhead of the decoding layers, but notably using the same operations as before. Similarly, Ref. [17] points out the first squeezing demonstrated on an optical transition with a Wineland squeezing parameter of 4.4(6) dB with ≈ 360 atoms. We directly measure a Wineland squeezing parameter [25] of 5.29(5) dB below the standard quantum limit using only 26 particles with the (1, 2) sequence. Second, the robustness of the scheme with respect to variations of the prior width (Fig. 4) enables reliable operation when shot-per-shot measurements exhibit fluctuations in the number of particles as commonly encountered in cold atom experiments.

The direct (offline) and on-device approaches to optimization we have demonstrated here are complimentary, and offer the benefits of the scheme to a variety of sensing tasks and platforms. The extremely narrow linewidth drive sources [26] and high operational fidelities of e.g. ion clocks can fully leverage the obtainable scheme benefits by direct implementation of the classically simulable variational parameters. The ‘self-calibrating’ approach on the other hand opens the scheme up for application in systems that are less well-characterized or where optimal parameters are classically intractable. For some types of native resources this ‘self-calibration’ is essentially the only viable route to optimization, such as for finite-range interactions in ultra-cold atoms [27]. Here we have chosen generalized Ramsey interferometry as an example application due to its prevalence in metrology. Through Ramsey or Ramsey-like sequence alone magnetic field [28], inertia [29], displacement and electric fields [30], as well as force measurements [31] are natural candidates to leverage the metrological gains afforded by the variational quantum circuit paradigm.

[1] Kaubruegger, R., Vasilyev, D. V., Schulte, M., Hammerer, K. & Zoller, P. Quantum Variational Optimization of Ramsey Interferometry and Atomic Clocks. *arXiv:2102.05593* (2021).

[2] Wineland, D. J. & Itano, W. M. Laser cooling of atoms. *Phys. Rev. A* **20**, 1521 (1979).

[3] Wineland, D. J., Bollinger, J. J., Itano, W. M., Moore, F. & Heinzen, D. Spin squeezing and reduced quantum noise in spectroscopy. *Phys. Rev. A* **46**, R6797 (1992).

[4] Leibfried, D. *et al.* Toward Heisenberg-limited spectroscopy with multiparticle entangled states. *Science* **304**, 1476–1478 (2004).

[5] Aasi, J. *et al.* Enhanced sensitivity of the LIGO gravitational wave detector by using squeezed states of light. *Nat. Photonics* **7**, 613–619 (2013).

[6] Giovannetti, V., Lloyd, S. & Maccone, L. Quantum-enhanced measurements: beating the standard quantum limit. *Science* **306**, 1330–1336 (2004).

[7] Tóth, G., Knapp, C., Gühne, O. & Briegel, H. J. Spin squeezing and entanglement. *Phys. Rev. A* **79**, 042334 (2009).

[8] Sewell, R. *et al.* Magnetic sensitivity beyond the projection noise limit by spin squeezing. *Phys. Rev. Lett.* **109**, 253605 (2012).

[9] Roos, C. F., Chwalla, M., Kim, K., Riebe, M. & Blatt, R. ‘Designer atoms’ for quantum metrology. *Nature* **443**, 316–319 (2006).

[10] Bollinger, J. J., Itano, W. M., Wineland, D. J. & Heinzen, D. J. Optimal frequency measurements with maximally correlated states. *Phys. Rev. A* **54**, R4649 (1996).

[11] Demkowicz-Dobrzański, R., Jarzyna, M. & Kolodyński, J. *Quantum Limits in Optical Interferometry*, vol. 60 of *Progress in Optics* (Elsevier, 2015).

[12] Pezzè, L., Smerzi, A., Oberthaler, M. K., Schmied, R. & Treutlein, P. Quantum metrology with nonclassical states of atomic ensembles. *Rev. Mod. Phys.* **90**, 035005 (2018).

[13] Demkowicz-Dobrzański, R., Kolodyński, J. & Gučă, M. The elusive heisenberg limit in quantum-enhanced metrology. *Nat. Commun.* **3**, 1–8 (2012).

[14] Degen, C. L., Reinhard, F. & Cappellaro, P. Quantum sensing. *Rev. Mod. Phys.* **89**, 035002 (2017).

[15] Macieszczak, K., Fraas, M. & Demkowicz-Dobrzański, R. Bayesian quantum frequency estimation in presence of collective dephasing. *New J. Phys.* **16**, 113002 (2014).

[16] Kitagawa, M. & Ueda, M. Squeezed spin states. *Phys. Rev. A* **47**, 5138 (1993).

- [17] Pedrozo-Peñaflor, E. *et al.* Entanglement on an optical atomic-clock transition. *Nature* **588**, 414–418 (2020).
- [18] Bohnet, J. G. *et al.* Quantum spin dynamics and entanglement generation with hundreds of trapped ions. *Science* **352**, 1297–1301 (2016).
- [19] Smith, A. F. A general Bayesian linear model. *J. R. Stat. Soc.* **35**, 67–75 (1973).
- [20] Leroux, I. D. *et al.* On-line estimation of local oscillator noise and optimisation of servo parameters in atomic clocks. *Metrologia* **54**, 307–321 (2017).
- [21] Schulte, M., Lisdat, C., Schmidt, P. O., Sterr, U. & Hammerer, K. Prospects and challenges for squeezing-enhanced optical atomic clocks. *Nat. Commun.* **11**, 1–10 (2020).
- [22] Pogorelov, I. *et al.* Compact Ion-Trap Quantum Computing Demonstrator. *PRX Quantum* **2**, 020343 (2021).
- [23] Takamoto, M., Takano, T. & Katori, H. Frequency comparison of optical lattice clocks beyond the tick limit. *Nat. Photonics* **5**, 288–292 (2011).
- [24] Schioppo, M. *et al.* Ultrastable optical clock with two cold-atom ensembles. *Nat. Photonics* **11**, 48–52 (2017).
- [25] Wineland, D. J., Bollinger, J. J., Itano, W. M. & Heinzen, D. Squeezed atomic states and projection noise in spectroscopy. *Phys. Rev. A* **50**, 67 (1994).
- [26] Kessler, T. *et al.* A sub-40-mHz-linewidth laser based on a silicon single-crystal optical cavity. *Nat. Photonics* **6**, 687–692 (2012).
- [27] Kaubruegger, R. *et al.* Variational spin-squeezing algorithms on programmable quantum sensors. *Phys. Rev. Lett.* **123**, 260505 (2019).
- [28] Jones, J. A. *et al.* Magnetic field sensing beyond the standard quantum limit using 10-spin noon states. *Science* **324**, 1166–1168 (2009).
- [29] Bordé, C. J. Atomic clocks and inertial sensors. *Metrologia* **39**, 435 (2002).
- [30] Gilmore, K. A. *et al.* Quantum-enhanced sensing of displacements and electric fields with large trapped-ion crystals. *arXiv:2103.08690* (2021).
- [31] Gilmore, K. A., Bohnet, J. G., Sawyer, B. C., Britton, J. W. & Bollinger, J. J. Amplitude sensing below the zero-point fluctuations with a two-dimensional trapped-ion mechanical oscillator. *Phys. Rev. Lett.* **118**, 263602 (2017).
- [32] André, A., Sørensen, A. & Lukin, M. Stability of atomic clocks based on entangled atoms. *Phys. Rev. Lett.* **92**, 230801 (2004).
- [33] Górecki, W., Demkowicz-Dobrzański, R., Wiseman, H. M. & Berry, D. W. π -corrected heisenberg limit. *Phys. Rev. Lett.* **124**, 030501 (2020).
- [34] Chabuda, K., Leroux, I. D. & Demkowicz-Dobrzański, R. The quantum Allan variance. *New J. Phys* **18**, 083035 (2016).
- [35] Borregaard, J. & Sørensen, A. S. Near-Heisenberg-limited atomic clocks in the presence of decoherence. *Phys. Rev. Lett.* **111**, 090801 (2013).
- [36] Leroux, I. D. *et al.* On-line estimation of local oscillator noise and optimisation of servo parameters in atomic clocks. *Metrologia* **54**, 307 (2017).

METHODS

M1. Optimized unitaries and dynamic range

In Ramsey interferometry we aim to estimate the interferometer phase ϕ from a measurement record of outcomes m , using a phase estimator ϕ_{est} . Specifically, we wish to find the mean value of ϕ , and minimize the measured imprecision or variance. Given m , typically particle excitations, and a phase estimator $\phi_{\text{est}}(m)$ we can find an estimate of the mean phase. The phase estimator ϕ_{est} may be any suitable function of the measurement outcomes m that approximates the phase in the region of interest, but is typically a linear function $\phi_{\text{est}}(m) = am$ with slope a [32]. This slope is often chosen as $a = (\partial_\phi \langle J_y \rangle |_{\phi=0} / \hbar)^{-1}$. In this work, a is not fixed but a free optimization parameter instead.

To gauge the imprecision we require the conditional probability $p(m|\phi)$ of measuring m for a phase ϕ . These conditional probabilities are generated as expectation values of projective measurements after the Ramsey sequence $\mathcal{U}_{\text{Ramsey}}$ has been applied to the initial state. In our measurement scheme with variational quantum circuits this sequence is given by

$$\mathcal{U}_{\text{Ramsey}}(\phi) = \mathcal{R}_x(\pi/2) \mathcal{U}_{\text{De}}(\boldsymbol{\vartheta}) \mathcal{R}_z(\phi) \mathcal{U}_{\text{En}}(\boldsymbol{\theta}) \mathcal{R}_y(\pi/2). \quad (1)$$

It is made up from unitary operators \mathcal{U}_{En} and \mathcal{U}_{De} that are defined by

$$\mathcal{U}_{\text{En}} = \prod_{k=1}^{n_{\text{En}}} \mathcal{R}_x(\theta_k^3) \mathcal{T}_x(\theta_k^2) \mathcal{T}_z(\theta_k^1) \quad (2)$$

$$\mathcal{U}_{\text{De}} = \prod_{k=1}^{n_{\text{De}}} \mathcal{T}_z(\vartheta_k^1) \mathcal{T}_x(\vartheta_k^2) \mathcal{R}_x(\vartheta_k^3), \quad (3)$$

and where the $\{\theta_k^i, \vartheta_k^i\}$ are the variational parameters forming vectors $\boldsymbol{\theta}$ and $\boldsymbol{\vartheta}$. The parameters n_{En} and n_{De} are the circuit layer depths, and are summarized as $(n_{\text{En}}, n_{\text{De}})$. The source operations $\mathcal{R}_{x,y,z}$ and $\mathcal{T}_{x,y,z}$ are rotation and twisting unitaries have which have the form

$$\mathcal{R}_{x,y,z}(\beta) = e^{-i\beta J_{x,y,z}} \quad (4)$$

$$\mathcal{T}_{x,y,z}(\chi) = e^{-i\chi J_{x,y,z}^2} \quad (5)$$

where β and χ are angles that depends on the interaction strength and time, and $J_{x,y,z}$ are angular momentum operators in the Cartesian basis. For the choice $(n_{\text{En}} = 0, n_{\text{De}} = 0)$ or $\boldsymbol{\theta} = \boldsymbol{\vartheta} = 0$ it follows that $\mathcal{U}_{\text{En}} = \mathcal{U}_{\text{De}} = 1$ and $\mathcal{U}_{\text{Ramsey}}$ is a standard Ramsey sequence.

Given the conditional probabilities we may quantify measurement imprecision using an error metric such as the mean square error (MSE) of the phase with respect to the phase estimator. It may be defined as

$$\text{MSE}(\phi) = \sum_m [\phi - \phi_{\text{est}}(m)]^2 p_{\boldsymbol{\theta}, \boldsymbol{\vartheta}}(m|\phi). \quad (6)$$

Minimization of the error metric is a central objective of metrology. This is achieved by tailoring the phase estimator ϕ_{est} and the conditional probability $p(m|\phi)$. However, $p(m|\phi)$ is both periodic in ϕ and the distribution's width is non-uniform over its period. The first means an interferometer has only limited *dynamic range* with respect to phase measurements (range of phases within which outcomes m can be assigned non-ambiguously), while the second relates to the interferometer *sensitivity* to different phases (slope $(\partial_\phi \langle J_y \rangle / \hbar)^{-1}$). A suitable gauge of interferometer performance should weigh this MSE more strongly where the interferometer sensitivity is greatest, and should weigh contributions at low sensitivity or outside of its dynamic range less. In the approach we explore here this is achieved by weighing the mean square error with a Bayesian prior distribution $P_{\delta\phi}(\phi)$ which encodes the statistical properties of the parameter, used sensor, and the measurement scheme. In particular, we focus on the relevant case of normal prior distributions, which has been studied in the literature [15], where

$$P_{\delta\phi}(\phi) = \frac{1}{\sqrt{2\pi\delta\phi^2}} \exp\left[-\phi^2/(2\delta\phi^2)\right], \quad (7)$$

with the prior width $\delta\phi$. Combining the prior and MSE yields the integral Bayesian mean square error, which is a function of only optimizer parameters and can thus be used to define cost in optimization schemes such as ours. If we define the BMSE as an operational cost as

$$\mathcal{C}(\boldsymbol{\theta}, \boldsymbol{\vartheta}, a) = \int d\phi \text{MSE}(\phi) P_{\delta\phi}(\phi), \quad (8)$$

then its minimum for a set of variational parameters is denoted as

$$\begin{aligned} (\Delta\phi)^2 &= \min_{\boldsymbol{\theta}, \boldsymbol{\vartheta}, a} \mathcal{C}(\boldsymbol{\theta}, \boldsymbol{\vartheta}, a) \\ &= \min_{\boldsymbol{\theta}, \boldsymbol{\vartheta}, a} \sum_m \int d\phi (\phi - am)^2 p_{\boldsymbol{\theta}, \boldsymbol{\vartheta}}(m|\phi) P_{\delta\phi}(\phi). \end{aligned} \quad (9)$$

Notably, the linear phase estimator slope a is chosen to optimize the BMSE, rather than the sensitivity to measurements at $\phi = 0$ as frequently done.

The prior distribution width $\delta\phi$ can be related to experimental system parameters, specifically the width of the distribution of expected phases after a Ramsey interrogation time T_R subject to a noisy reference laser. For noise power spectrum of bandwidth b_α and noise power spectral density $S(f) \propto f^{1-\alpha}$ the functional form is given by

$$\delta\phi = (b_\alpha T_R)^{\alpha/2}. \quad (10)$$

M2. Effects of resource restrictions

The globally optimal variational parameter sets depend on the ion number via the prior width. However,

we may additionally restrict them based on platform constraints of fundamental or practical nature to find sets optimal with respect to device capabilities. This adds to the adaptability inherent to the scheme: We tailor the cost function to the sensing task, and the sequence resources, while parameter ranges are constrained by the experimental hardware. Combined this assists with assessing and interpretation of attainable results given real-world constraints.

Furthermore, in systems of moderate size of order 50 and above this leads to the Allan deviation scaling down with particle number N or Ramsey time T_R at close to the (π -corrected) Heisenberg limit [33] up to a logarithmic correction [34, 35]. This is of great practical utility in situations where measurements are made with a fixed budget in particle number or measurement time.

M3. Allan deviation

In atomic clock settings we can link the BMSE $(\Delta\phi)^2$ to established figures of merit for frequency metrology, such as the Allan deviation. For clock operation without dead time and with averaging time τ these quantities may be related by

$$\sigma(\tau) = \frac{1}{\omega_A} \frac{\Delta\phi_M}{T_R} \sqrt{\frac{T_R}{\tau}} = \frac{1}{\omega_A} \frac{\Delta\phi_M}{T_R \sqrt{n}} \quad (11)$$

$$\Delta\phi_M = \Delta\phi / \sqrt{1 - \left(\frac{\Delta\phi}{\delta\phi}\right)^2} \stackrel{\delta\phi \rightarrow 0}{=} \sqrt{\frac{\xi_W^2}{N}}, \quad (12)$$

where $\Delta\phi_M$ is the effective measurement uncertainty of one cycle of clock operation [36], ξ_W is the Wineland parameter [25], n is the number of measurements per averaging time, and ω_A is the (atomic) reference frequency. The last equality holds as long as the Allan variance is dominated by projection noise, and will break down once the contribution from laser coherence becomes appreciable.

Limits to the Allan variance included in Fig. 2 d are the standard quantum limit, Heisenberg limit, and coherence time limits for a coherent spin state and the optimal quantum clock. The functional form of these lines in the units above for a flicker frequency noise power spectral density are:

$$\sigma_{\text{SQL}} = (\delta\phi N)^{-\frac{1}{2}} \quad (13)$$

$$\sigma_{\text{HL}} = (\delta\phi N^2)^{-\frac{1}{2}} \quad (14)$$

$$\sigma_{\text{CTL, CSS}} = \sqrt{\frac{1}{\delta\phi} (\sinh \delta\phi^2 - \delta\phi^2)} \quad (15)$$

$$\sigma_{\text{CTL, OQC}} = \sqrt{\frac{4\pi^2}{\delta\phi} \left(1 - \text{erf} \frac{\pi}{\sqrt{2}\delta\phi}\right)}, \quad (16)$$

where erf is the error function, and we assume $\delta\phi = b_\alpha T_R$. σ_{SQL} and σ_{HL} dominate for clocks limited by projection

noise, that is small $\delta\phi$, while $\sigma_{\text{CTL, CSS}}$ and $\sigma_{\text{CTL, OQC}}$ account for the particle number-independent coherence time limit imposed by laser noise fluctuations.

Data availability

All data obtained in the study is available from the corresponding author upon reasonable request.

Acknowledgements

We gratefully acknowledge funding from the EU H2020-FETFLAG-2018-03 under Grant Agreement no. 820495. We also acknowledge support by the Austrian Science Fund (FWF), through the SFB BeyondC (FWF Project No. F7109), and the IQI GmbH. This project has received funding from the European Union's Horizon 2020 research and innovation programme under the Marie Skłodowska-Curie grant agreement No 840450. P.S. acknowledges support from the Austrian Research Promotion Agency (FFG) contract 872766. P.S., T.M. and R.B. acknowledge funding by the Office of the Director of National Intelligence (ODNI), Intelligence Advanced Research Projects Activity (IARPA), via US ARO grant no. W911NF-16-1-0070 and W911NF-20-1-0007, and the US Air Force Office of Scientific Research (AFOSR) via IOE Grant No. FA9550-19-1-7044 LASCEM.

R.K., D.V., R.v.B. and P.Z. are supported by the US Air Force Office of Scientific Research (AFOSR) via IOE Grant No. FA9550-19-1-7044 LASCEM, the European Union's Horizon 2020 research and innovation program under Grant Agreement No. 817482 (PASQuanS) and No. 731473 (QuantERA via QTFLAG), and the Austrian Research Promotion Agency (FFG) contract 884471 (ELQO), and by the Simons Collaboration on Ultra-Quantum Matter, which is a grant from the Simons Foundation (651440, P.Z.), and by the Institut für Quanteninformation. Innsbruck theory is a member of the NSF Quantum Leap Challenge Institute Q-Sense.

All statements of fact, opinions or conclusions contained herein are those of the authors and should not be construed as representing the official views or policies of the funding agencies.

Author contributions

Ch.D.M. wrote the manuscript with input from co-authors. Ch.D.M., T.F., and I.P. built the experiment. Ch.D.M. and T.F. performed measurements. R.K., D.V., and P.Z. conceived of the method and provided theory. R.K. and R.v.B. developed the optimizer routines and implementation. Ch.D.M. and R.K. analysed the data. P.S., R.B., and T.M. supervised the experiment.

Competing interests

The authors declare no competing interests.

Supplementary Material

Supplementary Information is available for this paper.

Appendix S1: State preparation and readout

In the AQTION platform $^{40}\text{Ca}^+$ ions are hosted in a Paul trap forming a linear ion crystal under appropriate cooling. Optical qubits are encoded in the ground state $|4\text{S}_{1/2}, m_J = -1/2\rangle$ and excited state $|3\text{D}_{1/2}, m_J = -1/2\rangle$, which are connected via an electric quadrupole transition near 729 nm.

Further lasers at 397 nm, 854 nm, and 866 nm are required for state preparation and cooling. All ions are prepared in the qubit ground state via optical pumping before the start of each Ramsey sequence. The chain is cooled close to the motional ground state using resolved sideband cooling. Readout of the qubit system is performed optically via state-selective fluorescence near 397 nm, rendering the ground state bright and excited state dark. We perform site-selective readout of each ion using spatially-resolved detection on a camera through a high-numerical-aperture objective solely to increase detection fidelity; the scheme itself requires only collective measurements. All qubit operations as part of the Ramsey sequence are performed via a single laser beam oriented along the ion chain. The beam is aligned to interact identically with all ions.

Appendix S2: Implementation and calibration of unitaries

Qubit rotations $\mathcal{R}_{x,y}$ are implemented via resonant excitation on the qubit transition. The relative phase of pulses used to implement driven excitations sets the basis in which the rotation takes place, where a phase shift of $\pi/2$ changes between x and y . \mathcal{R}_z rotations may be implemented using AC Stark shifts induced by off-resonant excitation, but are not required here.

The infinite-range one axis twistings are implemented using the Mølmer-Sørensen interaction, whose unitary propagator takes the form $\exp(-i\chi\hat{J}_x^2)$ once appropriate conditions are met [1]. The interaction is generated by a bichromatic light field detuned from the ion chain's first axial center-of-mass vibrational sidebands by Δ_{MS} . An optical phase shift is again used to change between the x and y basis. Negative rotation angles may be implemented by inverting both tones' detunings with respect to the chosen mode's sidebands, but we restrict ourselves to positive twisting angles for ease of implementation.

The twisting angles implemented by the Mølmer-Sørensen interactions are given by the geometric phase χ enclosed during the operation. It is challenging to optimize this phase to an arbitrary value given that it has no easily accessible observable associated with it. Additionally, we require that the Mølmer-Sørensen operation leave no residual spin-motional entanglement which puts further conditions on experimental parameters that achieve any given value of χ . Consequently, our strategy has two steps. First, we optimize a fully entangling Mølmer-Sørensen gate which implements a geometric phase of $\chi = \pi/2$ and creates a GHZ state. The state fidelity of the GHZ state allows for careful calibration of χ at this value. After this, we scale all parameters relative to the obtained values as required to maintain loop closure to the desired geometric phases.

In particular, we close eight loops in phase space after the $\tau_{\text{MS}} = 1600 \mu\text{s}$ gate duration. A single loop in $200 \mu\text{s}$ at the same detuning thus implements a twisting angle of $\pi/16$. All required twisting angles are then obtained from this calibration by scaling the gate duration and detuning together fixing $\tau_{\text{MS}} = 2\pi/\Delta_{\text{MS}}$, noting that then $\chi \propto \tau_{\text{ms}}^2$. The laser-induced AC Stark shifts during the Mølmer-Sørensen interaction are mitigated using power imbalancing [2] rather than centerline detuning. This dramatically reduces the complexity of the sequences since these phase shifts depend on the twisting angles, which are varied across the sequences, thus requiring individual measurement and compensation.

The proposal's original unitaries contain twisting operations partly along the z axis. Unfortunately, \mathcal{T}_z cannot be natively implemented using the Mølmer-Sørensen interaction. However, we may use a simple basis change on the entire sequence to transform into solely using \mathcal{T}_x and \mathcal{T}_y . The Ramsey sequence unitary then takes the form

$$\mathcal{U}'_{\text{Ramsey}} = \mathcal{U}_{\text{De}}^{x,y} \mathcal{R}_y(\phi) \mathcal{U}_{\text{En}}^{x,y} \mathcal{R}_y(\pi/2), \quad (\text{S21})$$

where the superscripts indicate the two bases used for twisting and rotation. In atomic clock settings the phase ϕ accumulated due to a detuning from the atomic reference frequency leads to a rotation $\mathcal{R}_z(\phi)$, which may be implemented using the identity $\mathcal{R}_y(\phi) = \mathcal{R}_x(-\pi/2) \mathcal{R}_z(\phi) \mathcal{R}_x(\pi/2)$.

Appendix S3: Restrictions on sequence parameters

It is difficult to carefully calibrate twisting angles that differ strongly in magnitude. Consequently, we restrict the optimizer search to twisting angles $\varphi_{\min} \leq \varphi \leq \pi/8$. For small particle numbers, this comes at little cost to the predicted BMSE. φ_{\min} in turn is a lower bound on the twisting angles that is set by the minimal duration a Mølmer-Sørensen pulse can have in the experiment. This limitation is not set by experimental hardware, but instead by the pulse shaping necessary to minimize off-resonant carrier excitations [2]. φ_{\min} depends on the axial trap frequency, and we set it conservatively to

$\varphi_{\min} = \pi/160$. The absolute limit is near $\varphi_{\min} = \pi/576$ at which point the pulse will be entirely made up of shaping slopes. As an example, this $\pi/160$ limit means that 2 of the 6 twistings in the (1, 2) sequence are dropped for up to 26 ions. For the (1, 0) with up to 26 ions 1 of the 2 twistings are dropped.

Rotations are not in principle limited in this fashion, but due to technical constraints in the hardware must also have a minimum duration. We mitigate this by calibrating multiple rotation objects with different Rabi rates for large and small rotations. Rotation angles below a certain threshold will nonetheless be skipped, adding experimental error for small rotation angles.

Appendix S4: Experimental calculation of cost

The measurement record from the experiment is given by binary bit strings representing the z projections of the ion chain state during the measurement. An example would be a string 0010 = DDSD representing a four ion register where ions 1, 2, and 4 are in the excited D state and thus do not fluoresce, and ion 3 is in the bright ground state S.

For the measurement protocol we only require knowledge of collective measurement outcomes. Consequently, we calculate the probability $p(k|\phi_{\text{exp}})$ of finding k excitations among all bit strings for a given phase ϕ_{exp} from the histogram of outcomes. This is identical to finding the probability $p(m|\phi_{\text{exp}})$ to measure the excitation imbalance $m = (2k - N)/2$. Here ϕ_{exp} is the phase ϕ we want to implement up to a phase shift $\tilde{\phi}$ that arises in the implementation due to experimental imperfections such as timing jitter or residual AC Stark shifts.

To calculate the MSE and BMSE we require the phase estimator $\phi_{\text{est}} = am$, and knowledge of $\phi = \phi_{\text{exp}} - \tilde{\phi}$ to obtain the conditional probabilities at the true phase ϕ . To do this, we use the raw measurement data to calculate the conditional excitation imbalance probabilities and the MSE with both slope a and $\tilde{\phi}$ as free parameters, at a fixed grid of phase values. The parameter-dependent MSE errors are integrated using the Simpson rule and the resulting BMSE is minimized in terms of the free parameters. Typically we find $\tilde{\phi} \lesssim 0.01$, and the slope a is close to the theoretically predicted value. As an example, Tab. III shows $1/a$ for the $\delta\phi = 1$ data point in Fig. 2 c.

$(n_{\text{En}}, n_{\text{De}})$	Exp. $1/a$	Theory $1/a$
(0, 0)	4.731(12)	4.745
(1, 0)	4.363(9)	4.378
(0, 2)	3.042(4)	3.001
(1, 2)	3.023(4)	2.963

Table III. Comparison of linear phase estimator slopes a determined experimentally via numerical optimization of raw data and from theory for $\delta\phi = 1$ data in Fig. 2 c.

The cost function evaluation during the optimization is accelerated by measuring at ϕ values chosen to coincide

with the nodes of the Hermite-Gaussian polynomials up to twelfth order. We further leverage the symmetry of the MSE around $\phi = 0$ to perform Hermite-Gauss quadrature (HGQ) integration for $\phi \geq 0$ only. The HGQ proves particularly useful if only a small number of ϕ points is used for the numerical integration, where equidistantly spaced integration schemes can lead to a biased estimate of the cost function.

Appendix S5: Optimizer and meta-model design and tuning

On-device optimization is essentially a classical optimization problem, with data generated on a quantum machine. This is a well-studied problem for which several solutions have been demonstrated [3]. For the optimization we employ a modified version of the Dividing Rectangles algorithm (DIRECT) [4–6] which is a gradient-free algorithm that guarantees global convergence for sufficiently many iterations. DIRECT divides the search space into hyperrectangles, which we will refer to as ‘cells’. Each cell is represented by a single cost function evaluation taken in its interior. Promising cells are sampled at a finer scale by subdividing further, prioritizing cells with low cost function values, as well as cells with large size.

During the optimization the algorithm maintains an internal representation, denoted meta-model, of the cost function landscape in the form of a Gaussian process [7], modelling the data as jointly-distributed Gaussian variables with a trigonometric covariance kernel. For this meta-model we may expand the cost for each gate in a series of trigonometric functions of the interaction parameter since all interactions in the sequence are global. The cost function is then a product of $3(n_{\text{En}} + n_{\text{De}})$ trigonometric series which generally have non-vanishing expansion coefficients and argument scalings for both even and odd terms. The number of terms in each series as well as the scalings depend on the differences of eigenvalues of the generators of the gate, that is the differences of eigenvalues of $J_{x,y,z}$, and $J_{x,y,z}^2$. For rotations, these differences grow linearly in number, while for twistings they grow quadratically. The number of terms and scalings are known a priori for a given number of particles, so the cost has $6(n_{\text{En}} + n_{\text{De}})$ free parameters whose optimal match to the experimental data is continuously adapted with incoming measurement data.

The algorithm is provided with a finite measurement budget that it can spend during the optimization process. We invest only a relatively low number of measurements at each point to use the budget economically. If the variance of the cost function measurements is above a certain threshold, the algorithm can request refinement steps at points already sampled in order to increase the probability of correctly deciding which cells to subdivide. The algorithm selects when to perform the refinement steps, and how many measurements to spend in this stage.

These decisions are based on methods from decision theory and optimal computing budget allocation [5, 8].

To start the optimization we initialize search boxes ranging from 50 % to 150 % of the theoretically optimal parameter values. This situation is representative if there is some degree of trust in the operations implemented on the quantum machine. We further expect that for classically not simulatable resources, like finite range interactions, the optimal parameters will smoothly change with the particle number, allowing one to extrapolate similar constraints for the search space. We initialize the search by adding a random displacement to search box relative to the theoretical optimum to prevent the optimization algorithm from trivially finding the theoretically optimal parameters by initially sampling the parameter space in the center of the search box.

Appendix S6: Coarse and fine optimizer scans

Any optimizer intrinsically requires many evaluations of the same parameter landscape over time. In real experiments the quantum operations are subject to drift. Consequently, we perform ‘coarse’ evaluations to speed up the procedure with fewer repetitions (typically 100) per point and fewer sampling points in ϕ per evaluation (typically 5 - 11 nodes). Once a good parameter candidate has been identified, the optimizer requests a ‘fine’ scan of these parameters with finer sampling (typically 20 or 21 nodes) on both sides of $\phi = 0$, and more repetitions (typically 250).

Longer ion chains are subject to more frequent collisions with background gas in the trap than smaller chains, leading to frequent melting of the crystal. A molten crystal has to be recrystallized before the next state initialization can begin - a process typically referred to as refreezing. Refreezing the crystal takes substantially longer than state preparation and sequence execution. Refreeze events requiring remeasuring of a given point are more frequent in long chains, and fine scans with many repetitions per measurement point on long chains can thus become time consuming. Additionally, a detected refreeze event will discard all measured repetitions and start the measurement process anew. We alleviate this problem by batching measurement requests from the optimizer into multiples of 50-repetition measurements, so the maximum number of discarded measurements is 50.

Appendix S7: Noise frequency reconstruction

We try to reconstruct the known value of injected noise (detuning) by performing phase estimation with two different Ramsey sequences, while also accounting for the drift in the laser’s reference cavity.

A frequency detuning $\Delta\omega$ is drawn at random from a normal distribution with width $\Delta\omega_N = 2\pi \cdot 40 \text{ Hz}$ and

added to the laser frequency using an acousto-optic modulator. The distribution is truncated at $2\Delta\omega_N$ to reduce the influence of rare large detunings on the measurement outcome from the limited statistics of 200 different samples per Ramsey time.

We perform three Ramsey sequences successively where we impart the phase ϕ via $\mathcal{R}_x(-\pi/2)\mathcal{R}_z(\phi = \Delta\omega T_R)\mathcal{R}_x(\pi/2)$, with a detuning $\Delta\omega$: First, a standard Ramsey sequence without detuning ($\Delta\omega = 0$), with $T_R = 15$ ms and averaging over 50 repetitions. This is used to correct for the slow drift of our qubit laser's cavity. Second, 50 measurements with detuning $\Delta\omega$ using a standard CSS Ramsey sequence where the Ramsey time is varied and the laser frequency is estimated from evaluation of single measurements. Lastly, a sequence optimized for a prior width $\delta\phi = 0.6893$ with depths (1, 2) is used analogously to the second CSS sequence. This value is chosen as the equivalent Ramsey time at which both the CSS and the optimized sequence approximately have their respective minima in the BMSE. We repeated this measurement 200 times for each Ramsey time. The order of CSS and (1, 2) sequence was reversed after 100 repetitions to exclude a systematic bias, but no difference in outcome was found.

To explain the difference between the ideal measurement and our experiment we identify three main sources of error: First, frequency flicker noise of our laser. To determine the frequency noise we perform the measurement described above, without detuning $\Delta\omega$. For long Ramsey times the standard deviation of the measured

frequencies converges to $b_\alpha \approx 2\pi \cdot 6$ Hz. Second, the non-ideal BMSE measured in our system. Third, the BMSE increases with detuning $\Delta\omega$, so that the distribution width $\Delta\omega_N$ is a compromise between reducing the influence of laser frequency noise on the measurement ($\Delta\omega \gg b_\alpha$) and avoiding gate errors to achieve the best BMSE ($\Delta\omega \rightarrow 0$). Consequently the achievable gain is directly correlated to the laser frequency noise.

We note that the deterioration of the BMSE with detuning is an artifact of our measurement. In an optical clock the detuning $\Delta\omega$ is small and T_R is consequently much larger to reach the same $\delta\phi$. The large values of $\Delta\omega$ here cause deterioration of the gate-based implementation of the twistings, which is based in the technical limitations of the implementation, not the scheme itself.

Appendix S8: Sequence overhead

The variational sequences contain more operations than the archetypical Ramsey sequence, which produces time overhead in state preparation and measurement relative to the coherent spin state interferometer. These effects are typically negligible for high-precision trapped-ion or atomic systems, in particular for atomic clocks, where Ramsey times of order 1 s are reached. Even in our case the increase in sequence length accounts for less than 10 % of the state preparation time, below the gain in T_R . Specifically, for the sequences (1, 0) (SSS) our overhead is 165 μ s, the (1, 2) takes an additional 250 μ s, and (2, 1) (GHZ) takes 300 μ s extra compared to the CSS.

[1] Roos, C. F. Ion trap quantum gates with amplitude-modulated laser beams. *New J. Phys.* **10**, 013002 (2008).

[2] Kirchmair, G. *et al.* Deterministic entanglement of ions in thermal states of motion. *New J. Phys.* **11**, 023002 (2009).

[3] Cerezo, M. *et al.* Variational quantum algorithms (2020). 2012.09265.

[4] Jones, D. R., Perttunen, C. D. & Stuckman, B. E. Lipschitzian optimization without the lipschitz constant. *J. Optim. Theory Appl.* **79**, 157–181 (1993).

[5] Nicholas, P. A dividing rectangles algorithm for stochastic simulation optimization. In *Proc. Informs. Comput. Soc. Conf.*, vol. 14, 47–61 (2014).

[6] Kokail, C. *et al.* Self-verifying variational quantum simulation of lattice models. *Nature* **569**, 355–360 (2019).

[7] Rasmussen, C. E. *Gaussian Processes in Machine Learning* (Springer Berlin Heidelberg, Berlin, Heidelberg, 2004).

[8] Fu, M. C., Chen, C.-H. & Shi, L. Some topics for simulation optimization. In *Proceedings of the 40th Conference on Winter Simulation*, 27–38 (Winter Simulation Conference, 2008).